

Article

# Current-Mode Control of a Distributed Buck Converter with a Lossy Transmission Line

Klaus Röbenack <sup>\*,†</sup>  and Daniel Gerbet <sup>†</sup> 

Institute of Control Theory, Faculty of Electrical and Computer Engineering, TUD Dresden University of Technology, 01062 Dresden, Germany; daniel.gerbet1@tu-dresden.de

\* Correspondence: klaus.roebenack@tu-dresden.de

† These authors contributed equally to this work.

**Abstract:** This article presents a buck converter in which the inductor has been replaced by a transmission line. This approach would be practically conceivable if the power supply and load had a greater spatial distance. Alternatively, the model derived in this way could also be regarded as an intermediate model in order to replace a power coil via discretization with a larger number of smaller coils and capacitors. In the time domain, this new converter can be described by a system of coupled partial and ordinary differential equations. In the frequency domain, a transcendental transfer function is obtained. For comparison with an equivalently parameterized conventional converter, Padé approximants are derived. A linear controller is designed for the converter topology under consideration.

**Keywords:** switched-mode power supply; buck converter; step-down converter; transmission line; distributed systems; Padé approximants; PI control



**Citation:** Röbenack, K.; Gerbet, D. Current-Mode Control of a Distributed Buck Converter with a Lossy Transmission Line. *Electronics* **2024**, *13*, 3565. <https://doi.org/10.3390/electronics13173565>

Academic Editor: Jen-Hao Teng

Received: 29 June 2024

Revised: 31 August 2024

Accepted: 5 September 2024

Published: 8 September 2024



**Copyright:** © 2024 by the authors. Licensee MDPI, Basel, Switzerland. This article is an open access article distributed under the terms and conditions of the Creative Commons Attribution (CC BY) license (<https://creativecommons.org/licenses/by/4.0/>).

## 1. Introduction

Switched-mode power supply has become increasingly popular in recent decades. Its applications range from small electronic devices to the electrical power grid. In the field of home electronics and mobile devices, switched-mode DC/DC converters have almost completely replaced the linear regulators that were previously used.

Like other power supplies, switched-mode converters transfer power from a source to a load. In many cases, a desired output voltage must be set, but other targets such as current or power can also be specified. A buck converter (step-down converter) is used to provide a lower output voltage, while a boost (step-up converter) converter is used to provide a higher output voltage. Certain converter types, such as buck–boost converters or Ćuk converters, are able to provide both lower and higher output voltages [1].

Switched-mode DC/DC converters store the energy from the power supply temporarily in reactive network elements, i.e., inductors and capacitors, and then, release that energy to the load at a different voltage. The largest and most material-intensive component of the converter is typically the inductor, i.e., the choke. In [2–4], the power inductor was replaced by a transmission line resulting in distributed converter models. In [5–7], both the inductor and the capacitor were replaced by a transmission line. In other publications, the connection of conventional switched-mode converter circuits (i.e., with discrete reactive elements) to the load via transmission lines is investigated [8,9].

In Refs. [2,3], mathematical models were first derived for some converter circuits with a transmission line. This was followed by a spatial discretization of this transmission line. The approach leads to a lumped model in which the power inductor is replaced by several smaller coils and capacitors. The motivation for [4,6,7] was different. If the power supply and the load are physically separated, wired energy transmission is unavoidable. The idea behind the work was to replace reactive network elements with this supply line, which was needed anyway. In the buck converter, the transmission line can in principle replace

both the inductor and the capacitor. In the boost converter, the switch is located between the two elements so that the transmission line can only replace the coil. An experimental verification of these concepts with practical implementations was carried out in [2,3] and also in [6,7].

The modeling of conventional converter circuits initially leads to differential algebraic equations that can be reduced to ordinary differential equations [1]. After linearization, if necessary, a rational transfer function is obtained in the frequency domain. The modeling of a transmission line leads to partial differential equations which, if further discrete reactive network elements are present, have to be combined with ordinary differential equations [10,11]. In the frequency domain, this results in a transcendental transfer function, which typically contains exponential or hyperbolic functions.

Numerous control concepts have been investigated for conventional converter circuits, both linear and nonlinear, e.g., [1,12–14]. In practical applications, linear controllers are dominant [1,15,16]. Controller design for the class of distributed converter models, i.e., converters with a transmission line, is significantly more challenging due to the different type of mathematical models; e.g., see [17–19].

In this paper, we investigate a modified buck converter, where the inductor is replaced by a transmission line. Unlike previous work [5–7], the transmission line does not replace the capacitor. This approach leads to a significantly lower first resonance frequency compared to previous work. The modified buck converter is also considered in the frequency domain. For this model, a transcendental transfer function is derived and its rational approximations are discussed. In addition, we design a linear controller based on the conventional converter model with equivalent parameters. On the one hand, this approach can be used as in [2,3] to replace a power coil with a larger number of smaller components. On the other hand, an actual implementation of a converter with a transmission line for large-scale structures (e.g., supplying smaller consumers in a spacious property) or for ultra-light flying objects would be conceivable.

The paper is structured as follows: In Section 2, we derive mathematical models for the conventional and the distributed buck converter in the time as well as the frequency domain. The transient simulation of these converter models is discussed in Section 3. A description in the frequency domain and the behavior of the models under periodic excitation is investigated in Section 4. In Section 5, we present the controller design and simulate the closed-loop control system. Our results are discussed in Section 6.

## 2. Buck Converter Modeling

### 2.1. Lumped-Parameter Model of the Standard Buck Converter

The circuit diagram of the standard buck converter topologies are shown in Figure 1. The buck converter is a switched-mode power supply designed to reduce an input voltage to a lower output voltage. The switching is often carried out by a transistor in combination with a freewheeling diode, as shown in Figure 1 (left). This topology is known as an asynchronous buck converter. In our circuit diagram, we show an N-channel metal–oxide–semiconductor field-effect transistor (MOSFET), but one could also use a bipolar junction transistor (BJT) or an insulated-gate bipolar transistor (IGBT). Sometimes the diode is replaced by a second transistor, resulting in a synchronous buck converter, shown in Figure 1 (right). Both topologies are compared with regard to their efficiency in [20]. Furthermore, the converter consists of a coil (choke) and a capacitor. In this paper, the converter feeds a resistive load.

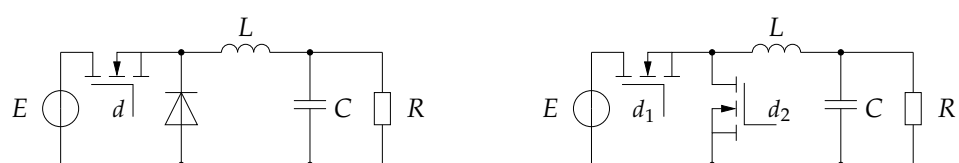


**Figure 1.** Circuit diagram of the asynchronous buck converter (left) and the synchronous buck converter (right).

From the schematics, we derive the network model shown in Figure 2. The supply voltage  $E$  is considered as an ideal constant voltage source. The semiconductor circuitry is modeled as a single-pole changeover switch with the two positions  $d = 0$  and  $d = 1$ . The coil is described by an inductance  $L$ , with conductor resistance  $R_L$ . The capacitor is modeled by a capacity  $C$ , with an insulation conductance  $G_C$ . The load is ohmic, with a resistance  $R$ .

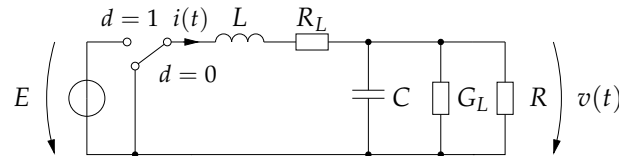


Figure 2. Network model of the standard buck converter considering losses.

From the network model we obtain the ordinary differential equations (ODEs)

$$L \frac{di(t)}{dt} + R_L i(t) + v(t) = E d(t) \tag{1}$$

$$C \frac{dv(t)}{dt} + \left(G_C + \frac{1}{R}\right)v(t) = i(t) \tag{2}$$

with  $L, C, R > 0$ , and  $R_L, G_C \geq 0$ . These ODEs constitute a lumped-parameter model in the time domain [21]. The ODEs can be transformed from the time to the frequency domain using the Laplace transform

$$\underbrace{\begin{pmatrix} sL + R_L & 1 \\ -1 & sC + G_C + \frac{1}{R} \end{pmatrix}}_{M(s)} \begin{pmatrix} I(s) \\ V(s) \end{pmatrix} = \begin{pmatrix} E \\ 0 \end{pmatrix} D(s), \tag{3}$$

where we use capital letters for the transformed signals and assume vanishing initial values, i.e.,  $i(0) = 0$  and  $v(0) = 0$ . For current-mode control we use (3) to derive the transfer function

$$P(s) = \frac{I(s)}{D(s)} = \frac{E \left(sC + G_C + \frac{1}{R}\right)}{LCs^2 + \left(LG_C + R_L C + \frac{L}{R}\right)s + 1 + R_L \left(G_C + \frac{1}{R}\right)} \tag{4}$$

from the switching signal  $D(s)$  to the current  $I(s)$ . This second-order transfer function corresponds to a damped harmonic oscillator. The stability property holds even in the case of lossless reactive network elements (i.e.,  $R_L = 0$  and  $G_C = 0$ ) due to the damping resulting from the load resistance  $R > 0$ . Therefore, the system is bounded-input bounded-output (BIBO)-stable for all physically meaningful parameter values.

### 2.2. Distributed-Parameter Model of the Buck Converter with Lossy Transmission Line

If there is a certain spatial distance between the voltage source and the load, then the electrical energy transmission could be described by a transmission line. This transmission line could also be used to replace the inductor. The second reactive element of the converter circuit, the capacitor, is present as a discrete component in parallel with the load. Replacing only one reactive element with the transmission line corresponds to the approach described in [2–4]. The circuit topology of the resulting converter is shown in Figure 3.

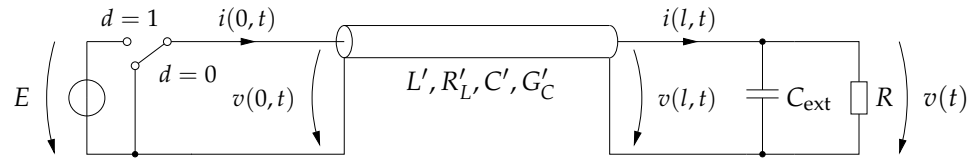


Figure 3. Distributed buck converter with transmission line.

The central part of the new converter topology is the transmission line, which can be modeled by the partial differential equations

$$L' \frac{\partial}{\partial t} i(z, t) + R'_L i(z, t) + \frac{\partial}{\partial z} v(z, t) = 0, \tag{5}$$

$$C' \frac{\partial}{\partial t} v(z, t) + G'_C v(z, t) + \frac{\partial}{\partial z} i(z, t) = 0 \tag{6}$$

known as telegrapher’s equations [10,11]. The current  $i$  and the voltage  $u$  along the transmission line depend both on the time  $t \geq 0$  and the spatial position  $z \in [0, l]$ , where  $l$  denotes the length of the transmission line. The parameters  $L'$ ,  $C'$ ,  $R'_L$ , and  $G'_C$  describe the inductance, capacitance, resistance, and conductance per length, respectively. These PDEs constitute a distributed-parameter model [21].

Both ends of the transmission line are connected to the remaining circuitry. Mathematically, these connections are described by boundary conditions. On the left-hand side, i.e., at  $z = 0$ , we have the input voltage  $E d(t)$  resulting from the voltage source and the switch. On the right-hand side, i.e., at  $z = l$ , we have the parallel circuit of the external capacitor  $C_{ext} > 0$  and the ohmic load  $R > 0$ . This leads to the Robin boundary conditions

$$v(0, t) = E d(t) \tag{7}$$

$$C_{ext} \dot{v}(l, t) + \frac{1}{R} v(l, t) = i(l, t) \tag{8}$$

because the second condition is specified by a linear combination of the voltage and its time derivative on the spatial boundary. Therefore, we can consider the overall model (5)–(8) as a coupled PDE-ODE system.

For further investigations we transform the PDE (5) and (6) from the time into the Laplace frequency domain:

$$(sL' + R'_L) I(z, s) + \frac{\partial}{\partial z} V(z, s) = 0, \tag{9}$$

$$(sC' + G'_C) V(z, s) + \frac{\partial}{\partial z} I(z, s) = 0, \tag{10}$$

where the spatial dependency remains unchanged. Similar to Section 2.1, we assume vanishing initial values, i.e.,  $i(\cdot, 0) = 0$  and  $v(\cdot, 0) = 0$ . We can rewrite (9) and (10) as a linear state-space model

$$\frac{\partial}{\partial z} \begin{pmatrix} I(z, s) \\ V(z, s) \end{pmatrix} = \underbrace{\begin{pmatrix} 0 & -(sC' + G'_C) \\ -(sL' + R'_L) & 0 \end{pmatrix}}_{A(s)} \underbrace{\begin{pmatrix} I(z, s) \\ V(z, s) \end{pmatrix}}_{X(z, s)}, \tag{11}$$

where the ODEs are formulated in terms of the spatial variable  $z$ . The characteristic equation

$$\det(\gamma I - A(s)) = \gamma^2 - (sL' + R'_L)(sC' + G'_C) = 0,$$

where  $I$  denotes the identity matrix, has the roots

$$\gamma_{1,2}(s) = \pm \sqrt{(sL' + R'_L)(sC' + G'_C)}. \tag{12}$$

In general, the solution of an initial-value problem of the linear system (11) can be written as

$$X(z, s) = \exp(A(s) z) X(0, s) \tag{13}$$

with the matrix exponential function

$$\exp(A(s) z) = \sum_{k=0}^{\infty} \frac{1}{k!} [A(s) z]^k. \tag{14}$$

Using the linear dependency

$$[A(s)]^2 = (sL' + R'_L)(sC' + G'_C) I = \gamma^2 I,$$

we can decompose the series expansion (14) into odd and even terms and obtain

$$\exp(A(s) z) = \cosh(\gamma z) I + \frac{1}{\gamma} \sinh(\gamma z) A. \tag{15}$$

For current-mode controller design, we want to describe the input–output relation on the left boundary (7), taking the right boundary condition (8) into account. In the Laplace domain, condition (8) can be written as

$$V(l, s) = Z(s) I(l, s) \quad \text{with} \quad Z(s) = R \parallel \frac{1}{sC_{\text{ext}}} = \frac{R}{1 + sRC_{\text{ext}}}, \tag{16}$$

where the impedance  $Z$  describes the parallel connection of  $R$  and  $C_{\text{ext}}$ . To describe the conditions on the left boundary, we solve (13) with respect to the initial vector

$$X(0, s) = \exp(-A(s) l) X(l, s) \tag{17}$$

and set  $z = l$  for the right boundary. The exponential matrix (14) is always invertible. In (17), the inverse exponential matrix results from the reverse spatial direction. Using (15), we have

$$\begin{aligned} M(s) := \exp(-A(s) l) &= \cosh(\gamma l) I - \frac{1}{\gamma} \sinh(\gamma l) A(s) \\ &= \begin{pmatrix} \cosh(\gamma l) & \frac{1}{\gamma}(sC' + G'_L) \sinh(\gamma l) \\ \frac{1}{\gamma}(sL' + R'_L) \sinh(\gamma l) & \cosh(\gamma l) \end{pmatrix}. \end{aligned}$$

With  $M = (m_{ij})$ , we can write (17) element-wise as

$$I(0, s) = m_{11}(s) I(l, s) + m_{12}(s) V(l, s) = [m_{11}(s) + m_{12}(s) Z(s)] I(l, s) \tag{18}$$

and

$$V(0, s) = m_{21}(s) I(l, s) + m_{22}(s) V(l, s) = [m_{21}(s) + m_{22}(s) Z(s)] I(l, s). \tag{19}$$

Combining (7), (18) and (19), we obtain the transfer function

$$\begin{aligned}
P(s) &= \frac{I(0,s)}{D(s)} \\
&= \frac{I(0,s)}{V(0,s)} E \\
&= \frac{m_{11}(s) + m_{12}(s) Z(s)}{m_{21}(s) + m_{22}(s) Z(s)} E \\
&= \frac{(sC' + G'_C) Z(s) \sinh(\gamma l) + \gamma \cosh(\gamma l)}{(sL' + R'_L) \sinh(\gamma l) + \gamma Z(s) \cosh(\gamma l)} E \\
&= \frac{(sC' + G'_C) R \sinh(\gamma l) + \gamma(1 + sRC_{\text{ext}}) \cosh(\gamma l)}{(sL' + R'_L)(1 + sRC_{\text{ext}}) \sinh(\gamma l) + \gamma R \cosh(\gamma l)} E
\end{aligned} \tag{20}$$

from the duty ratio to the current into the transmission line.

On the one hand, we consider a lossy transmission line, resulting in a damped distributed-parameter part. On the other hand, the lumped-parameter part of the network is strongly damped by the load resistance. Therefore, the distributed converter model is also bounded-input bounded-output-stable. However, the resonance peaks in the higher-frequency range can result in a significantly higher gain compared to the conventional converter model; see Section 4.2.

### 3. Simulation Models

#### 3.1. Model Parameters

In this paper, we want to investigate a new converter topology and compare it with the standard buck converter. For this reason, the parameters for the distributed-parameter converter are determined first. The parameters of the lumped-parameter converter are then determined in an equivalent manner for a suitable comparison.

The central part of the new buck converter is the transmission line. In this paper, we consider the transmission line which was used in practical realizations discussed in [6,7]. In particular, we use an  $l = 6$  m coaxial cable RG 58 C/U [22]. The inductance and capacitance per length are  $L' = 241$  nH/m and  $C' = 100$  pF/m, respectively. While a lossless cable was considered in [6,7], the losses are taken into account in this publication. According to [23], the coaxial cable RG 58 C/U has a maximum conductor resistance of  $40.7 \Omega/\text{km}$ . For our considerations we assume  $R'_L = 40 \Omega/\text{km} = 40$  m $\Omega/\text{m}$ . Furthermore, the minimum insulation resistance is  $5 \text{ G}\Omega \times \text{km}$ , resulting in a conductance per length of  $G'_C = 0.2$  pS/m. These primary line constants result in the following integral values of the transmission line:

$$\begin{aligned}
\bar{L} &= l \cdot L' = 1446 \text{ nH}, \\
\bar{C} &= l \cdot C' = 600 \text{ pF}, \\
\bar{R}_L &= l \cdot R'_L = 240 \text{ m}\Omega, \\
\bar{G}_C &= l \cdot G'_C = 1.2 \text{ pS}.
\end{aligned} \tag{21}$$

In addition to the transmission line, the new converter possesses an external capacitor with the capacitance  $C_{\text{ext}} = 1 \mu\text{F}$ . In connection with (21), we define the following parameter values for the standard buck converter:

$$\begin{aligned}
L &= \bar{L} = 1446 \text{ nH}; \\
C &= \bar{C} + C_{\text{ext}} = 1000.6 \text{ nF}; \\
R_L &= \bar{R}_L = 240 \text{ m}\Omega; \\
G_C &= \bar{G}_C = 1.2 \text{ pS}.
\end{aligned} \tag{22}$$

Both converters are supplied with  $E = 12$  V and operated with the load  $R = 10 \Omega$ .

#### 3.2. State-Space Model of the Standard Buck Converter

We can rewrite the network Equations (1) and (2) as a two-dimensional state-space model:

$$\dot{x}(t) = A x(t) + B d(t), \quad y(t) = C x(t) + D d(t). \tag{23}$$

With the state vector  $x = (x_1, x_2)^T = (i, v)^T$ , the system matrix  $A \in \mathbb{R}^{2 \times 2}$ , the input matrix  $B \in \mathbb{R}^{2 \times 1}$ , the output matrix  $C \in \mathbb{R}^{2 \times 2}$  and the throughput matrix  $D \in \mathbb{R}^{2 \times 1}$  are given by

$$A = \begin{pmatrix} -\frac{R_L}{L} & -\frac{1}{L} \\ \frac{1}{C} & -\frac{1+R G_C}{RC} \end{pmatrix}, \quad B = \begin{pmatrix} \frac{E}{L} \\ 0 \end{pmatrix}, \quad C = \begin{pmatrix} 1 & 0 \\ 0 & 1 \end{pmatrix}, \quad D = \begin{pmatrix} 0 \\ 0 \end{pmatrix} \tag{24}$$

with the parameters listed in (22). The output matrix is a  $2 \times 2$  identity matrix such that both components of the state vector are available on the output for measurement. The throughput matrix is a zero matrix because the system does not have a direct throughput. Therefore, the output vector has the form

$$y(t) = x(t) = \begin{pmatrix} i(t) \\ v(t) \end{pmatrix}.$$

Consider a constant input signal  $d^0 \in [0, 1]$ . For a non-singular system matrix  $A$ , the state-space model (23) has an unique equilibrium point at

$$x^0 = -A^{-1} B d^0.$$

With the matrices (24), we obtain

$$x^0 = \begin{pmatrix} i^0 \\ v^0 \end{pmatrix} = \begin{pmatrix} \frac{(G_C R + 1) E}{G_C R R_L + R + R_L} d^0 \\ \frac{E R}{G_C R R_L + R + R_L} d^0 \end{pmatrix}. \tag{25}$$

From  $R, R_L, G_C > 0$  we conclude  $0 \leq v^0 < E$ , i.e., the voltage at the equilibrium point is always less than the supply voltage  $E$ .

By (25), the current and the voltage in the equilibrium point are specified by the input values  $d^0$ . In practice, a desired voltage is usually specified. For a prescribed reference  $v^0$ , the values of the reference current and the reference input are given by

$$i^0 = \frac{G_C R + 1}{R} v^0 \quad \text{and} \quad d^0 = \frac{(G_C R + 1) R_L + R}{E R} v^0. \tag{26}$$

### 3.3. State-Space Model of the Buck Converter with Transmission Line

To simulate the distributed converter, the transmission line is replaced by a spatially discretized network model. Figure 4 shows the resulting network model, where the integer  $N$  is the number of spatial discretization steps. The parameters  $\delta L$  and  $\delta R_L$  and  $\delta C$  and  $\delta G_C$  describe the inductance and the conductor resistance as well as the capacitance and insulation conductance per discretized element, respectively.

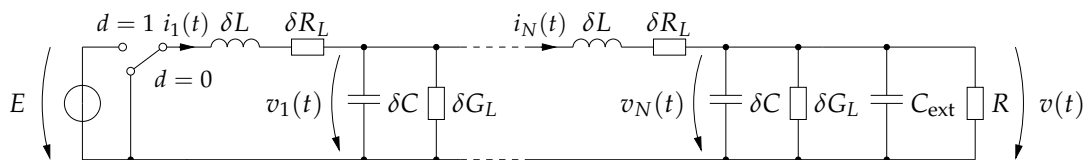


Figure 4. Distributed buck converter with discretized transmission line.

Kirchhoff's voltage law results in the network equations

$$\begin{aligned}
 \delta L \frac{d}{dt} i_1(t) + \delta R_L i_1(t) &= d(t) E - v_1(t), \\
 \delta L \frac{d}{dt} i_2(t) + \delta R_L i_2(t) &= v_1(t) - v_2(t), \\
 &\vdots \\
 \delta L \frac{d}{dt} i_{N-1}(t) + \delta R_L i_{N-1}(t) &= v_{N-2}(t) - v_{N-1}(t), \\
 \delta L \frac{d}{dt} i_N(t) + \delta R_L i_N(t) &= v_{N-1}(t) - v_N(t),
 \end{aligned}
 \tag{27}$$

and Kirchhoff's current law yields the further network equations

$$\begin{aligned}
 \delta C \dot{v}_1(t) + \delta G_C v_1(t) &= i_1(t) - i_2(t), \\
 \delta C \dot{v}_2(t) + \delta G_C v_2(t) &= i_2(t) - i_3(t), \\
 &\vdots \\
 \delta C \dot{v}_{N-1}(t) + \delta G_C v_{N-1}(t) &= i_{N-1}(t) - i_N(t), \\
 (\delta C + C_{\text{ext}}) \dot{v}_N(t) + \left( \delta G_C + \frac{1}{R} \right) v_N(t) &= i_N(t).
 \end{aligned}
 \tag{28}$$

These equations can be written as a state-space system (23). Defining the state vector

$$\mathbf{x} = \left( i_1 \quad i_2 \quad \dots \quad i_{N-1} \quad i_N \quad v_1 \quad v_2 \quad \dots \quad v_{N-1} \quad v_N \right)^T$$

we obtain the matrices  $A \in \mathbb{R}^{2N \times 2N}$ ,  $B \in \mathbb{R}^{2N \times 1}$ ,  $C \in \mathbb{R}^{2 \times 2N}$ , and  $D \in \mathbb{R}^{2 \times 1}$ , of the form

$$\left( \begin{array}{c|c} \mathbf{A} & \mathbf{B} \\ \hline \mathbf{C} & \mathbf{D} \end{array} \right), \tag{29}$$

Detailed description of matrix (29): The matrix is a 2N x (2N+1) block matrix partitioned into four quadrants: A (top-left, 2N x 2N), B (top-right, 2N x 1), C (bottom-left, 2 x 2N), and D (bottom-right, 2 x 1).  
 - **Block A (top-left):** A tridiagonal matrix with diagonal elements  $-\frac{\delta R_L}{\delta L}$  and off-diagonal elements  $-\frac{\delta R_L}{\delta L}$  between adjacent nodes. The bottom-right element is  $-\frac{\delta R_L}{\delta L} - \frac{1}{\delta C + C_{\text{ext}}}$ .  
 - **Block B (top-right):** A column vector with  $\frac{E}{\delta L}$  at the top, zeros for nodes 2 through N, and zeros for nodes N+1 through 2N.  
 - **Block C (bottom-left):** A row vector with  $\frac{1}{\delta C}$  at the first position,  $-\frac{1}{\delta C}$  at the second position, and zeros elsewhere.  
 - **Block D (bottom-right):** A column vector with  $\frac{1}{\delta C + C_{\text{ext}}}$  at the first position and zero at the second position.

The simulation model has two outputs. We use the first current and the last voltage of the discretized model (27) and (28). Again, the throughput matrix is a zero matrix because the system does not have a direct throughput. Hence, we have the output vector

$$\mathbf{y}(t) = \begin{pmatrix} i_1(t) \\ v_N(t) \end{pmatrix}.$$

In our simulation, we use  $N = 25$ . This results in the following parameters in the system matrices (29) of the discretized model:



$$\begin{aligned}
\delta L &= \bar{L}/N = 57.84 \text{ nH}; \\
\delta C &= \bar{C}/N = 24 \text{ pF}; \\
\delta R_L &= \bar{R}_L/N = 9.6 \text{ m}\Omega; \\
\delta G_L &= \bar{G}_C/N = 0.048 \text{ pS}.
\end{aligned}
\tag{30}$$

### 3.4. Open-Loop High-Level Simulation

In this section, we carry out open-loop high-level transient simulations of the converter models derived in Sections 3.2 and 3.3. These highly idealized models are used in power electronics to simulate the basic system behavior [1,24]. This means that these simulation results are independent of the semiconductor components used. For the numerical simulation we employ Scilab 2024 [25] with the graphical editor Xcos under Fedora Linux 39. The source files for the simulations will be available on Github [26] under the GNU General Public License v3.0.

Using the parameters given in Section 3.1, and taking the losses described by  $R_L$  and  $G_C$  into account, the largest output voltage that can be achieved continuously is  $v^0 \approx 11.72 \text{ V}$ , resulting from (25) with  $d^0 = 1$ . In our considerations, the buck converter should be operated in such a way that an output voltage of  $v^0 = 6 \text{ V}$  is produced. With (26), we obtain the reference input  $d^0 \approx 0.512$ . With this constant input signal, the current  $i^0 \approx 0.6 \text{ A}$  should be achieved asymptotically. For both converter models we used a zero vector of appropriate dimension as an initial value. Figure 5 shows the simulation results. The step response of the classic converter corresponds to a stable second-order oscillatory system due to its overshoot. The current of the discretized distributed converter oscillates with a higher frequency, around the current of the standard buck converter, as shown in Figure 5 (left). The output voltages of both converters match visually; see Figure 5 (right). The first voltage peak occurs at  $t \approx 3.78 \mu\text{s}$ , the second at  $t \approx 11.345 \mu\text{s}$ . Therefore, the declining oscillation has a period of approximately  $11.345 \mu\text{s} - 3.78 \mu\text{s} = 7.565 \mu\text{s}$ , which corresponds to a frequency of roughly  $1/7.565 \mu\text{s} \approx 132 \text{ kHz}$ .

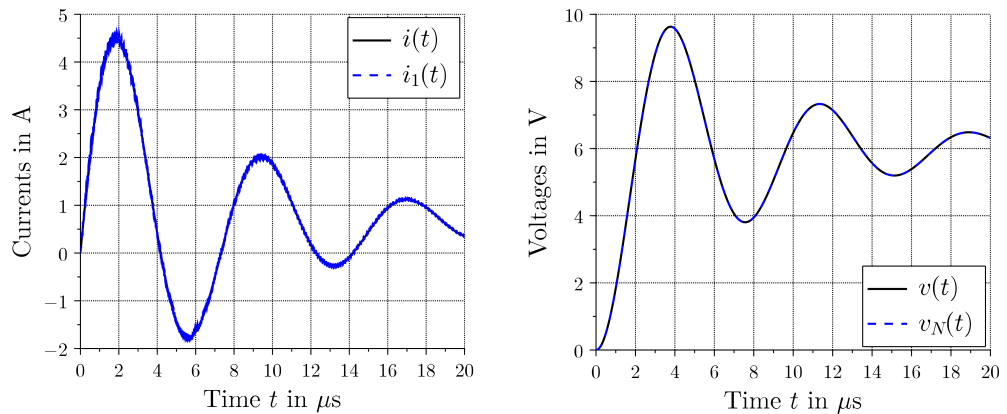


**Figure 5.** Step response of the state-space models of the standard and the discretized distributed buck converter.

While any value of the input signal  $d(t)$  can be applied to the linear continuous-time model (23), only discrete values  $d(t) \in \{0, 1\}$  are possible with the converter circuit. A pulse-width modulation (PWM) can be used to simulate continuous values in the interval  $d(t) \in [0, 1]$ . In particular, for a given number  $D \in [0, 1]$  the switching signal is generated by

$$d(t) = \begin{cases} 1 & \text{if } \text{mod}(t, T_{\text{PWM}}) \leq D T_{\text{PWM}} \\ 0 & \text{otherwise} \end{cases}
\tag{31}$$

with the switching time  $T_{\text{PWM}} > 0$  and the switching frequency  $f_{\text{PWM}} = 1/T_{\text{PWM}}$ . The number  $D$  is called the duty ratio or duty cycle [1]. In an analog implementation, the switching signal would be generated using a sawtooth or a triangular signal, as shown in Figure 6, and a comparator. In a digital implementation, counters are used.

Next, we simulated both converters under PWM excitation. To achieve the desired output voltage  $v^0 = 6\text{ V}$  we used the duty ratio  $D = d^0 \approx 0.512$ . The transient simulation results of the state-space models of the standard and the discretized distributed buck converter are shown in Figure 7. As initial vectors we used zero vectors of appropriate dimensions. The simulations were carried out for different PWM frequencies  $f_{\text{PWM}} \in \{2\text{ MHz}, 6\text{ MHz}, 10\text{ MHz}\}$ . For the discretized distributed converter, there are significant current ripples due to traveling waves in the transmission line, which tend to decrease with increasing PWM frequency. On the other hand, the voltage ripples can just about be seen at  $f_{\text{PWM}} = 2\text{ MHz}$ , but not at the higher frequencies used here. The voltage peaks are smoothed by the external capacitor. This represents a significant improvement compared to the investigations in [6,7].

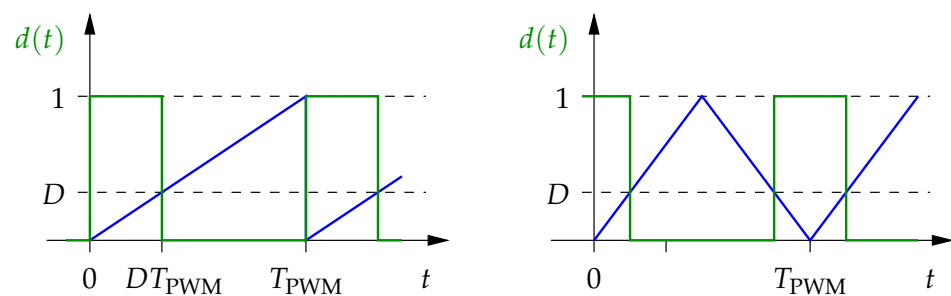


**Figure 6.** Analog PWM generation using a reference sawtooth signal (left) or a reference triangular signal (right) with the sawtooth as well as the triangular signal in blue and the PWM signal in green.

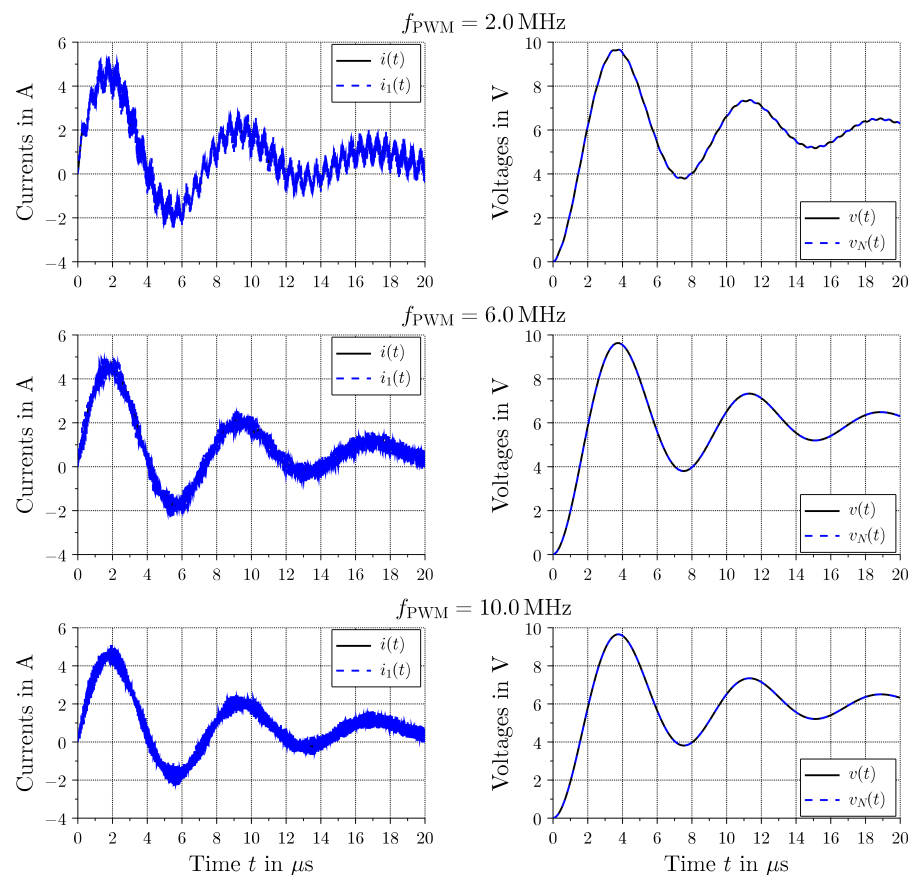


**Figure 7.** Responses of the state-space models of the standard and the discretized distributed buck converter under PWM excitation with different frequencies.

### 3.5. Open-Loop Circuit Simulation

Nowadays, circuit simulators are able to reproduce or predict the behavior of analog and digital circuits very precisely. We use the fast free circuit simulator LTspice® XVII (x64) provided by Analog Devices Inc. (Wilmington, MA, USA) [27]. The simulation results are visualized with Scilab 2024 [25].

Figure 8 shows the implementation of the distributed buck converter using LTspice®. The central element of the new converter topology is the lossy transmission line. In Spice, we have the following convention:

```
01 n1 n2 n3 n4 LOSSY
.model LOSSY LTRA(L=241e-9 C=100e-12 R=40e-3 len=6)
```

Here, 01 defines lossy transmission line #1 with a model named LOSSY. Furthermore, n1 and n2 are the nodes at port 1 and n3 and n4 are the nodes at port 2. The model LOSSY is an instance of the lossy transmission line model (LTRA) using the primary line parameters given in Section 3.1, with the exception of the line conductance  $G'_C$ , which is not yet implemented. Based on the parameter values used, however, it can be assumed that the influence of  $G'_C$  is considerably less than that of the conductor resistance  $R'_L$ . On the load side, R1 and C1 are connected to the transmission line. Without the comparatively large resistor R2 the transient simulation would stop with an error message as the reference potential on the load side seems not to be defined. The voltage source V5 with 0 V is introduced to measure the current into the transmission line.

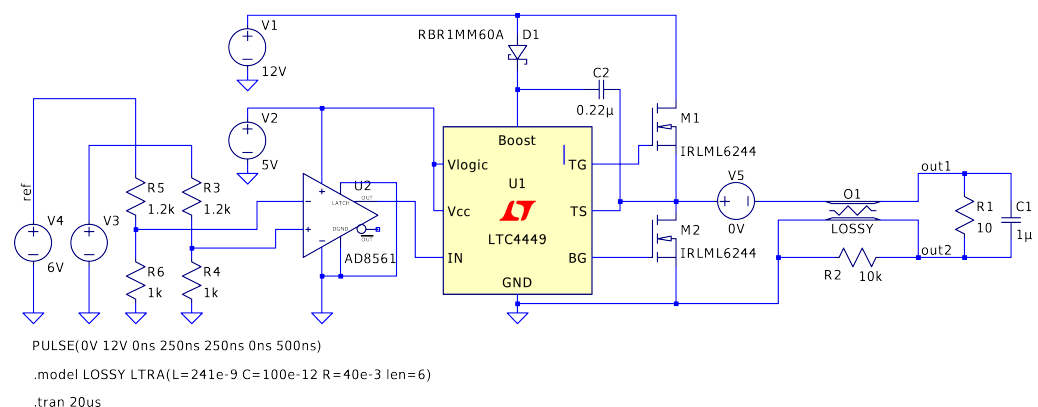


**Figure 8.** Implementation of open-loop buck converter with a lossy transmission line in LTspice®.

For switching we use the topology of a synchronous buck converter with two n-channel power MOSFETs IRLML6244. These transistors are actuated by the high-speed gate driver circuit U1 (LTC4449). The PWM signal is provided by the ultra-fast single-supply comparator U2 (AD8561). Voltage source V3 generates a triangular signal with a signal level of 12 V and a frequency of 2 MHz, defined by a rise and fall time of 250 ns and a period of 500 ns. In the lossless case, the voltage source V4 would be the desired reference voltage, where 6 V would correspond to the duty ratio  $d^0 = 0.5$ . To achieve an output voltage of 6 V, taking the lossy transmission line into account would require the above mentioned duty ratio  $d^0 = 0.512$ , leading to the reference voltage  $0.512 \times 12 \text{ V} = 6.144 \text{ V}$ . Figure 9 shows the input current and the output load voltage of the transmission line resulting from the transient simulation with LTspice®. These results show a qualitative agreement with the high-level simulation results shown in the first row of Figure 7. The generated data and the LTspice® schematic files are available on [26].

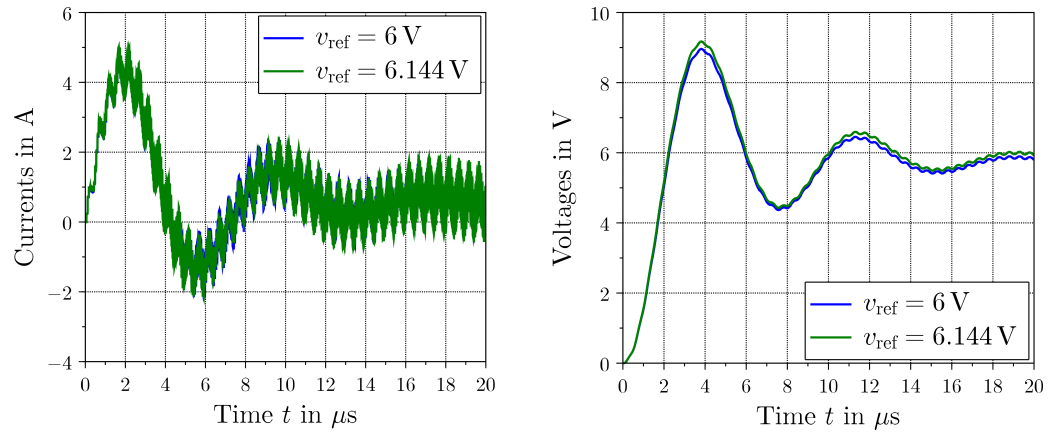


**Figure 9.** Open-loop circuit simulation results: input current (left) and output voltage (right) for different reference voltages.

### 4. Frequency Domain

#### 4.1. Transfer Function

The input–output behavior of the classical buck converter is described by the transfer function (4). Using the parameter values given in Section 3.1 we obtain

$$P(s) = \frac{8,298,755.186721992s + 829,377,891,946.9895}{s^2 + 265,915.1397140521s + 707,735,801,119.8038} \tag{32}$$

The transfer function is strictly proper. The (normalized) poles  $s_{1,2} \approx -132,957.57 \pm 830,697.35j$  are a conjugate pair located in the left half-plane. The step response of (32) should result in a declining oscillation, which is consistent with the numerical simulation carried out in Section 3.4; see Figure 5.

The transfer function for the distributed converter was derived in (20). We omit printing this transfer function with the numerical parameter values because the corresponding expression is very large. However, this transfer function is not rational, but transcendent. This property complicates controller design because many design methods require a rational transfer function of the plant. To avoid these difficulties we approximate the transcendent transfer function (20) by a rational function.

Given a transfer function  $P$ , the Padé approximant of order  $(m, n)$  is the rational function

$$P_{m,n}(s) = \frac{b_m s^m + \dots + b_1 s + b_0}{s^n + a_{n-1} s^{n-1} + \dots + a_1 s + a_0} \tag{33}$$

To obtain the Padé approximant (33) we expand the original function  $P$  in a Maclaurin series (i.e., a Taylor series at 0) with  $n + m$  coefficients:

$$P(s) = c_0 + c_1 s + \dots + c_{n+m} s^{n+m} + \mathcal{O}(s^{n+m+1}) \tag{34}$$

The coefficients  $a_0, \dots, a_{n-1}, b_0, \dots, b_m$  are calculated via coefficient matching between (33) and (34).

The Taylor expansion (34) required to calculate the Padé approximant (33) led to error messages in the computer algebra programs Maxima 5.45.1 [28] and SageMath 10.2 [29]. The issues with the series expansion most likely resulted from the term  $\gamma$ , which is a square root according to (12). In the series expansion of the functions occurring in (15), however, the term  $\gamma$  only occurs in even powers:

$$\begin{aligned} \cosh(\gamma z) &= 1 + \frac{1}{2} \gamma^2 z^2 + \frac{1}{24} \gamma^4 z^4 + \dots, \\ \frac{1}{\gamma} \sinh(\gamma z) &= z + \frac{1}{6} \gamma^2 z^3 + \frac{1}{120} \gamma^4 z^5 + \dots \end{aligned}$$

Note that these are entire functions in  $s$ . If these series expansions are used when calculating the transfer function (20), the problems mentioned above can be avoided as there is no longer a square root.

The RC element at the right boundary of the transmission line would tend to produce low-pass behavior, at least for high frequencies. This qualitative assumption leads to the requirement  $m < n$  for the Padé approximant (33), i.e., to a strictly proper transfer function. With SageMath 10.2 [29] we computed the following low-order Padé approximants of the transcendent transfer function (20):

$$P_{0,1}(s) = \frac{-121,684.784841855}{s - 103,837.683063803} \quad (35)$$

$$P_{1,2}(s) = \frac{8.30398290026456 \times 10^6 s + 8.29900199309498 \times 10^{11}}{s^2 + 265,983.502353863 s + 7.08181503402271 \times 10^{11}} \quad (36)$$

#### 4.2. Response under Sinusoidal Excitation

The Bode plot of the frequency responses of the derived transfer functions are shown in Figure 10. The amplitude responses of the classical and the distributed converter as well as its Padé approximant of order (1,2) agree up to  $\omega \approx 10^7$  rad/s. The transcendent transfer function (20) of the distributed converter shows a qualitatively different behavior for  $\omega \gtrsim 10^7$  rad/s. These three models have a resonance peak with an angular resonance frequency  $\omega_0 \approx 0.841 \times 10^6$  rad/s, corresponding to the technical frequency  $f_0 = \omega_0/2\pi \approx 134$  kHz. This is consistent with the frequency of the declining oscillations observed in the transient simulation in Section 3.4. Of course, the resonance peak cannot be described by the Padé approximant of order (0,1). In contrast, an antiresonance can only occur with the distributed converter model. The first angular antiresonance frequency occurring at  $\omega_1 \approx 53.3 \times 10^6$  rad/s corresponds to the technical frequency  $f_1 = \omega_1/2\pi \approx 8.49$  MHz. With increasing frequencies, resonances and antiresonances alternate for the distributed converter model. The second angular resonance frequency occurs at  $\omega_2 \approx 107 \times 10^6$  rad/s, i.e.,  $f_2 = \omega_2/2\pi \approx 17$  MHz. This is the first resonance frequency caused by the transmission line dynamics: The transmission line has the phase delay  $T_D \approx 29.46$  ns; see [4]. The resonance frequency corresponds to the time of a wave traveling forward and backward, i.e.,  $f_2 \approx 1/2T_D$ .

#### 4.3. Response under PWM Excitation

The frequency response is the gain factor of the system's steady-state response to harmonic (i.e., sinusoidal) excitations for different angular frequencies. However, in the case of switched converters, the excitation is not sinusoidal, but by means of PWM signals. The PWM signals are periodic and can be expanded into a Fourier series. The switching frequency is the fundamental frequency, but there are also higher harmonics that also depend on the duty cycle. The higher harmonics can possibly excite resonance frequencies in the higher-frequency spectrum. To investigate this problem we excited the discretized model of the distributed converter with different PWM signals. The transient simulations were carried out over a duration of 100  $\mu$ s. The ripples occur in the current transients as shown in Figure 6. To measure these ripples in a near steady-state situation, we computed the standard deviation  $\sigma$  of the current transients in the last 10% of the simulation time, i.e., for the range between  $t = 90$   $\mu$ s and  $t = 100$   $\mu$ s. To compare the results with the amplitude frequency response shown in Figure 10, the dependence of the standard deviation of the current on the angular PWM frequency  $\omega_{\text{PWM}} = 2\pi f_{\text{PWM}}$  is shown in Figure 11 using a logarithmic plot. We used a slightly smaller frequency range, as in Figure 10, but included the first angular resonance frequency  $\omega_0$  and the angular antiresonance frequency  $\omega_1$ .

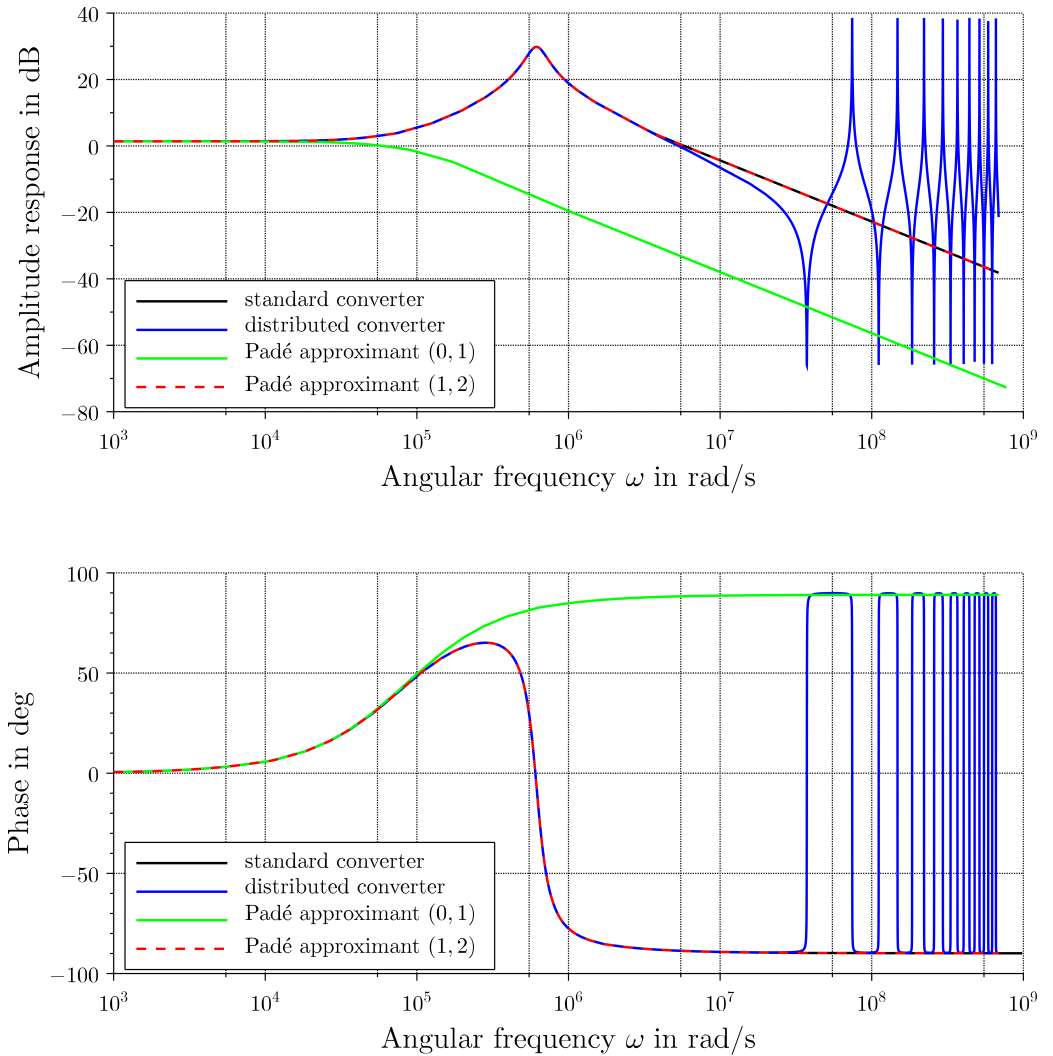


Figure 10. Bode plot of the frequency responses of the transfer functions.

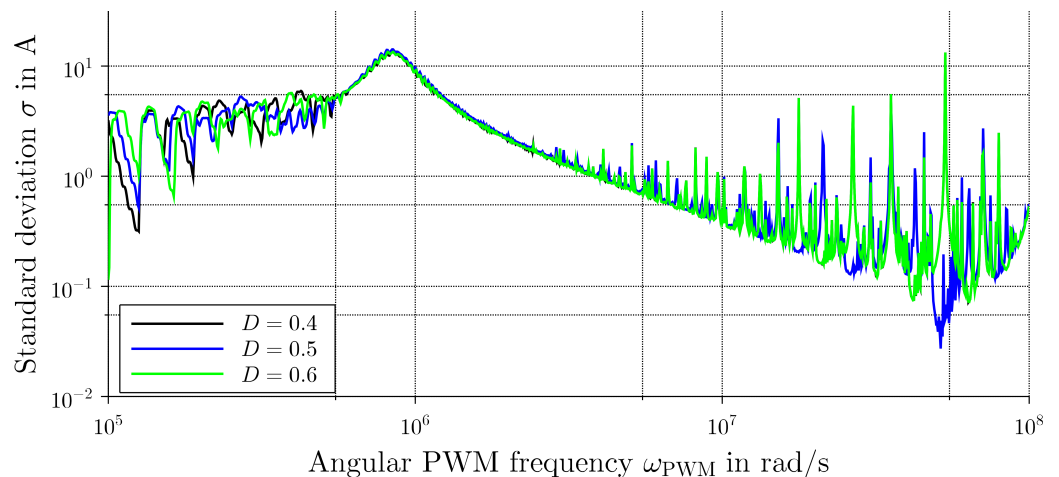
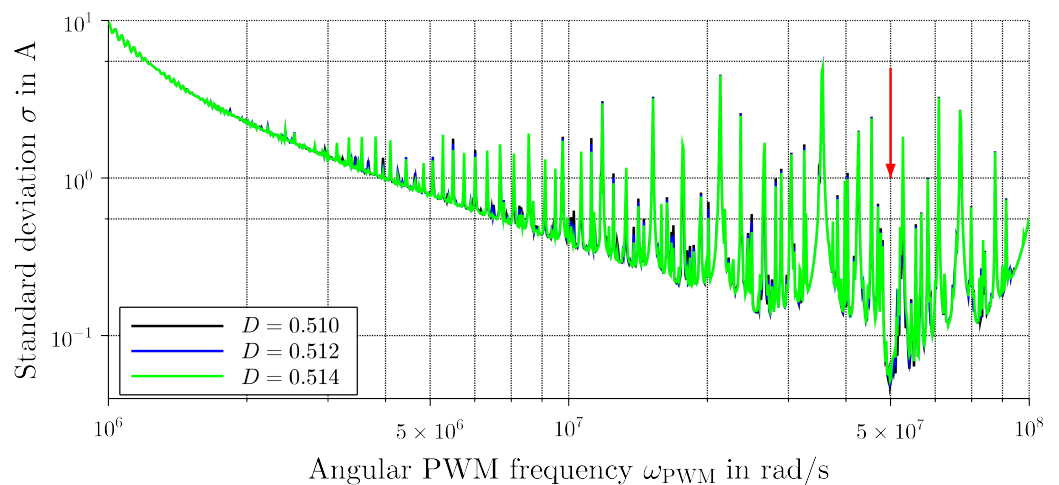


Figure 11. Standard deviation of the current peaks in the range between  $t = 90 \mu s$  and  $t = 100 \mu s$  of the simulated distributed converter under PWM excitation for duty ratios  $D \in \{0.4, 0.5, 0.6\}$ .

The curves shown in Figure 11 are roughly similar to the frequency response shown in Figure 10, especially near the first resonance frequency  $\omega_0$ . We plotted the standard deviation computed for different duty ratios  $D \in \{0.4, 0.5, 0.6\}$ , whereby there is a considerable qualitative similarity between the curves. Below the resonance frequency  $\omega_0$ , the low-pass

filter, which results from the line inductance, the external capacitor, and the load resistance, has hardly any effect. As a result, relatively large fluctuations occur in the standard deviation. From the resonance frequency  $\omega_{\text{PWM}} = \omega_0$  up to about  $\omega_{\text{PWM}} \approx 3 \times 10^6$  rad/s, a continuous drop in the standard deviation can be seen, which is due to the low-pass behavior. At higher frequencies, peaks occur more and more strongly, which can be explained by the forward- and backward-traveling waves in the transmission line in the time domain or by resonance peaks excited by higher harmonics in the frequency domain. We see a significant drop in the standard deviation near the antiresonance frequency  $\omega_1$  for  $D = 0.5$ . On the other hand, we have resonances for  $D = 0.4$  and  $D = 0.6$  in this frequency range. This can be explained as follows: Resonances and antiresonances alternate for multiples of the first antiresonance frequency. For  $D = 0.5$ , the Fourier series of the PWM signal (with the exception of the constant term) only contains odd coefficients. This means that only antiresonances are excited, so that current ripples are mostly suppressed. For  $D \neq 0.5$ , the Fourier series of the PWM signal also contains even harmonics, which excite resonances, and thus, lead to current ripples.

Figure 11 shows that the antiresonance frequency was different at different duty cycles. A more in-depth analysis is therefore necessary for the desired operating point. In Section 3.4, for the desired output voltage  $v^0 = 6$  V, the input signal  $d^0 \approx 0.512$  was determined based on an averaged model. For the switched model, the duty cycles  $D \in \{0.510, 0.512, 0.514\}$  that lie in the neighborhood of this operating point should therefore be considered. Figure 12 shows the standard deviation as a function of the angular PWM switching frequency for the range restricted to the higher frequencies. It can be seen that a significant reduction in the standard deviation is achieved in the region of  $\omega_{\text{PWM}} \approx 5 \times 10^7$  rad/s for all duty cycles considered. Here, there is obviously a noticeable antiresonance frequency. This frequency is marked with a red arrow in the diagram.



**Figure 12.** Standard deviation of the current peaks in the range between  $t = 90 \mu\text{s}$  and  $t = 100 \mu\text{s}$  of the simulated distributed converter under PWM excitation for duty ratios  $D \in \{0.510, 0.512, 0.514\}$ . The red arrow marks a noticeable antiresonance frequency.

## 5. Closed-Loop Control

### 5.1. Control Structure and Static Prefilter

The desired control variable is the output voltage  $v(l, t)$  on the right-hand side of the transmission line. For a useful implementation, the control and measurement should take place at the same side of the transmission line. A voltage is fed into the left-hand side of the transmission line via the PWM-controlled switch. It therefore makes sense to use the duty ratio  $D(t) \propto v(0, t)$  as the manipulated variable and the measured current  $i(0, t)$  as the feedback variable. In addition, the duty ratio is limited to  $D(t) \in [0, 1]$ . This restriction is ensured by a saturation block. The resulting structure of the closed control loop is shown

in Figure 13. The resulting input–output behavior of the plant has already been taken into account in the transfer function (20).

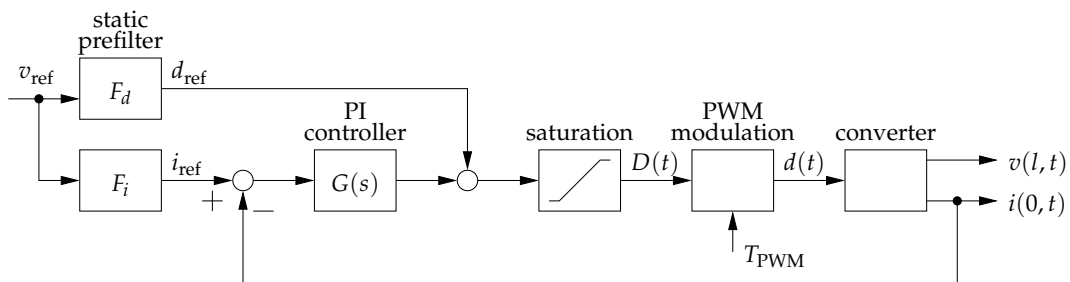


Figure 13. Closed-loop control structure.

The fact that we want to specify a reference voltage makes a conversion from voltage to the duty ratio and the current necessary. This conversion is performed via the static prefilters. From the equilibrium condition (26) of the finite dimensional model of the classical converter we obtain the scaling factors

$$F_i = \frac{(G_C R + 1)}{R} \approx \frac{1}{R} = \frac{1}{10 \Omega} = 0.1 \text{ S} \tag{37}$$

and

$$F_d = \frac{(G_C R + 1)R_L + R}{E R} \approx \frac{R_L + R}{E R} = \frac{1.024}{12 \text{ V}} = 0.0853 \text{ V}^{-1}. \tag{38}$$

The insulation losses  $G_C$  are extremely low and will therefore be neglected.

### 5.2. Controller Design

For angular frequencies up to  $\omega \approx 10^7$  rad/s, the frequency responses of the classic converter with discrete components and the converter with the transmission line agree very well, as shown in Section 4.2. The transfer function (4), respectively, (32), of the classic converter should therefore be used for a controller design in the frequency range, but then used for the distributed converter.

DC/DC converters are very often regulated with proportional–integral controllers (PI controllers); see, e.g., [1,15,16]. In the frequency domain, PI controllers can be described by the transfer function

$$G(s) = k \left( 1 + \frac{1}{sT_i} \right) \tag{39}$$

$$= k_p + \frac{k_i}{s}. \tag{40}$$

Equation (39) is the standard form of the PI controller with the gain  $k$  and the integral time constant  $T_i$ . This form is helpful for the controller design, whereas the parallel form (40) with the proportional gain  $k_p = k$  and the integral gain  $k_i = k/T_i$  is often used for implementation. If  $k_i = 0$ , we obtain a proportional controller (P controller).

There are many different methods and approaches for designing PI controllers [30,31]. Since the plant’s transfer function (32) is comparatively simple as a second-order system, we carry out the controller design directly in the frequency domain. For this reason, we consider the open-loop transfer function of the form

$$P(s) \cdot G(s) = k \frac{b_1 s + b_0}{s^2 + a_1 s + a_0} \cdot \frac{1 + sT_i}{sT_i}, \tag{41}$$

where the coefficients  $a_0, a_1, b_0, b_1$  result from the transfer function (32) of the plant. The transfer function (41) is unstable due to the integral part of the controller, which can be recognized by the pole at the origin. First of all, the closed-loop system should be stable.



In addition, the oscillations that occur in the plant should be suppressed in the closed control loop.

Due to the low inductance of the transmission line, the radian resonant frequency  $\omega_0$  of the equivalent conventional converter is comparatively high. In practice, the required settling times typically correspond to significantly lower frequencies. The integral time constant is selected with  $T_i = 10 \mu\text{s}$  such that the folding frequency  $\omega_i = 1/T_i = 10^5 \text{ rad/s}$  is approximately one order of magnitude below the resonance frequency. Figure 14 shows the Bode plot of the frequency responses of the plant's transfer function (32) as well as the open-loop transfer function (41) with  $k = 1$ . A discussion on the choice of the controller time constants can be found in Section 8.2.2 of [1].

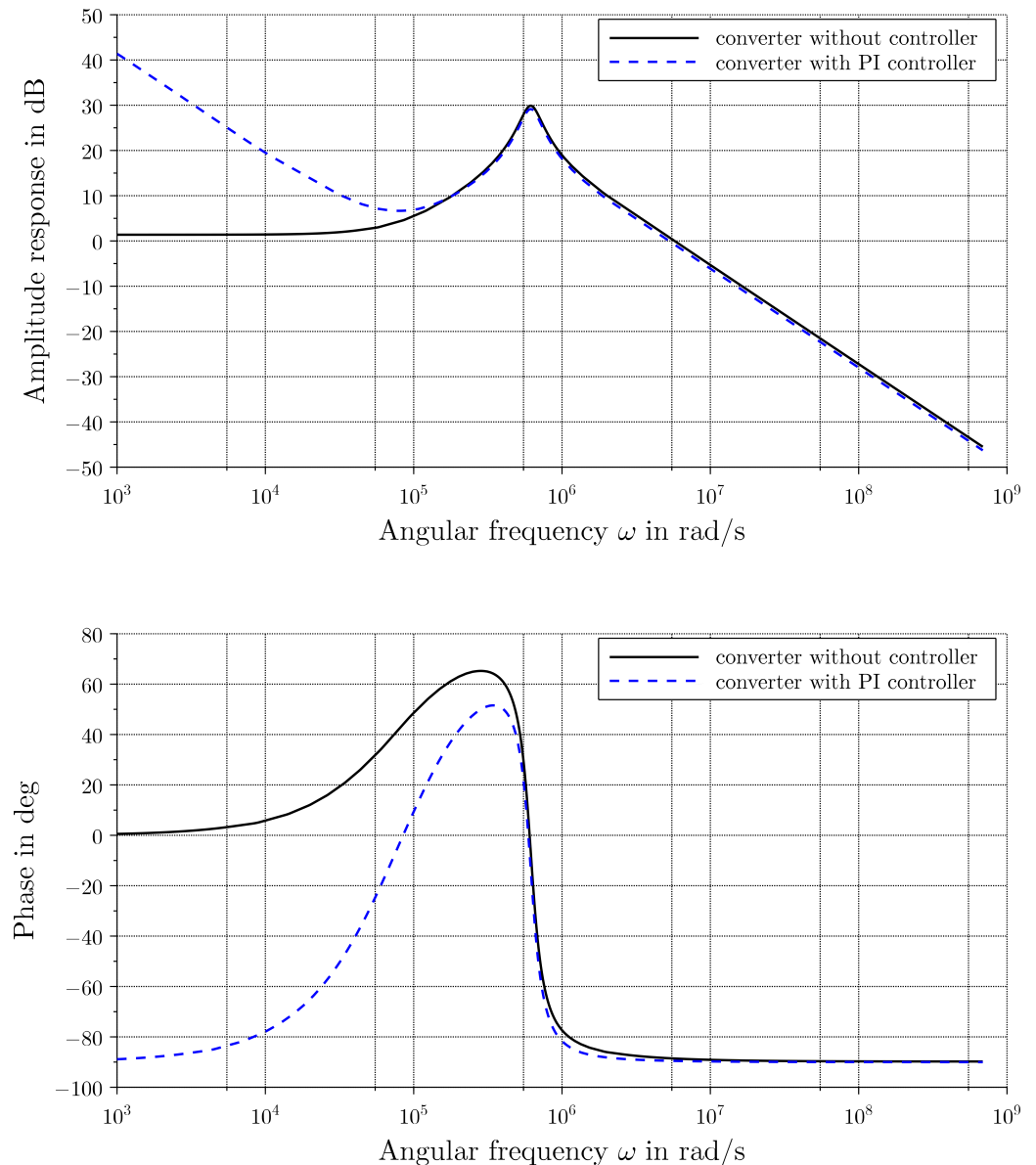


**Figure 14.** Bode plot of the frequency responses of the plant's transfer function (32) as well as the open-loop transfer function (41) including the PI controller with  $k = 1$ .

The gain  $k$  must still be determined for the PI controller. We use the root locus technique, which provides a design method based on the system's open-loop transfer function [32]. With this method, the poles of the closed-loop system are plotted in the complex plane as a function of the gain  $k$ .

The root locus plot of the open-loop transfer function (41) is shown in Figure 15. The root loci start for  $k = 0$  at the poles of the open-loop transfer function, i.e., at a conjugate complex pair located in the left half-plane resulting from the plant (32) and a pole in the origin resulting from the integral part of the PI controller. From  $k \gtrsim 0.214$ , the conjugate complex pole pair merges into two real poles on the real left half-axis. A double real pole occurs at this transition, whereby the associated gain can be calculated in Scilab using the function `krac2`. For  $k \rightarrow \infty$ , the root loci converge to the zeros of the open-loop transfer function. We have one real zero at  $s \approx -99,940$  due to the plant's transfer function (32) and another real zero at  $s = -1/T_i = -100,000$  from the PI controller. These zeros are located on the real left half-axis and cannot be distinguished visually in Figure 15. Two branches of the root locus plot converge to these zeros. Since the open-loop transfer function has one zero less than the poles, the third branch on the root locus plot converges to  $s \rightarrow -\infty$ .

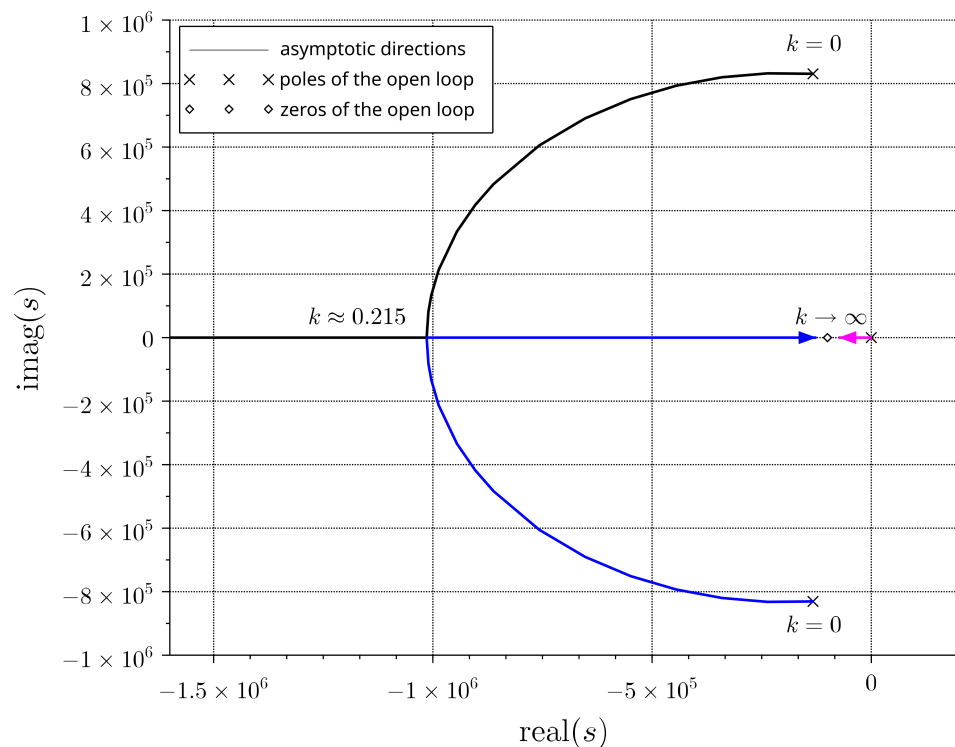


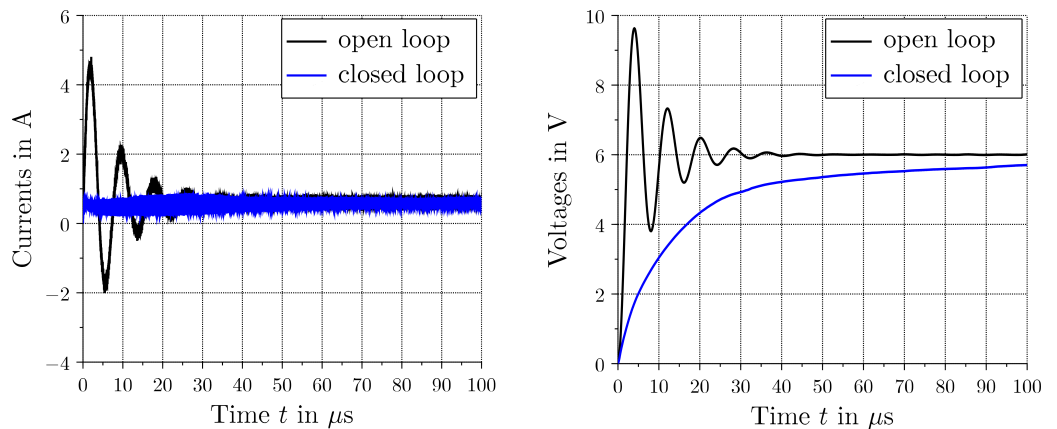
Figure 15. Root locus plot of (41) for  $k \geq 0$ .

From the root locus plot we draw the following conclusions: For any  $k > 0$  the closed-loop system is stable. With  $k \gtrsim 0.214$ , the system has solely real poles, i.e., so that no oscillations occur. In our simulation, we will use gain  $k = 1$ , resulting in a phase margin of slightly more than  $90^\circ$ . In general, the controller gain should not be set too high for buck converters, because the input saturation of the duty cycle may lead to a controller windup [33]. As an alternative to the proposed nominal design, the controller parameters could also be optimized using robust control methods [34].

### 5.3. Closed-Loop High-Level Simulation

The simulation is carried out on the discretized distributed converter model. The PWM frequency must still be defined for the simulation. The PWM frequency should be chosen such that current ripples are largely suppressed. In Section 4.3, we observed an antiresonance area around  $\omega_{\text{PWM}} \approx 5 \times 10^7$  rad/s. This leads to the technical PWM frequency  $f_{\text{PWM}} \approx 7.957747$  MHz. As with the simulations before, we want to obtain an output voltage of 6 V. The transient simulation results of the open and closed control loops of the discretized distributed buck converter are shown in Figure 16. The controller suppresses the oscillations that occur in the open control loop. The desired output voltage

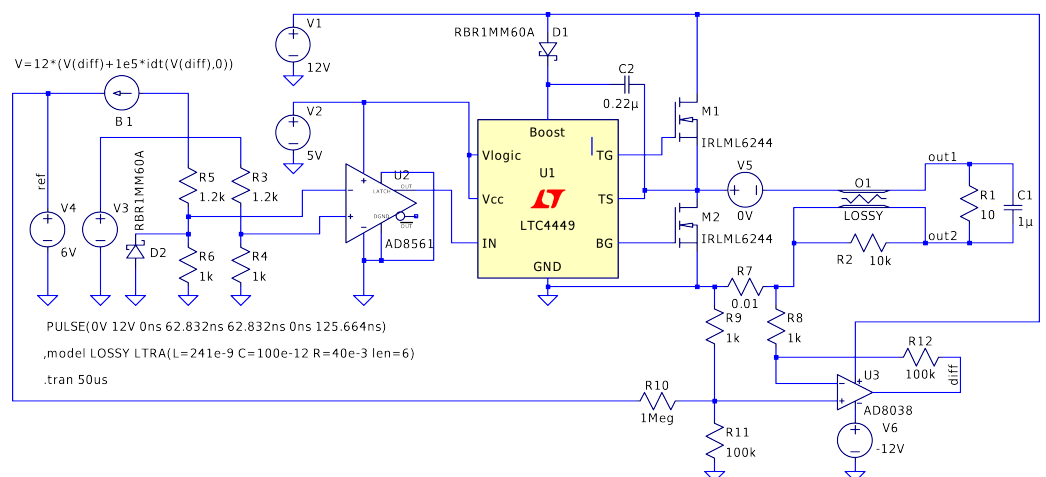
is achieved. There are only comparatively small ripples in the current. The controller designed for the classic converter also works with the distributed converter.



**Figure 16.** Transient high-level simulation of the state-space model of the discretized distributed buck converter in open and closed control loops.

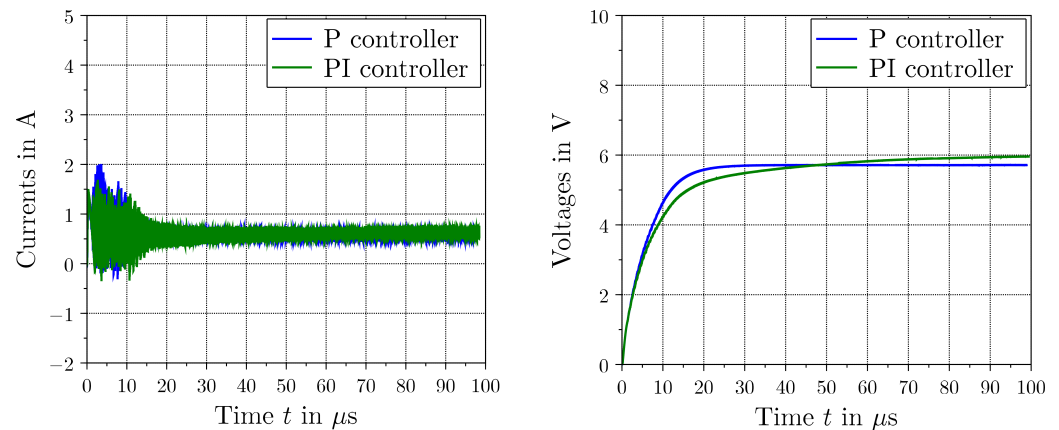
5.4. Closed-Loop Circuit Simulation

Figure 17 shows the circuit diagram of the closed-loop implementation of the buck converter with a lossy transmission line in LTspice®. For low-side current measurement, the 0.01 Ω shunt R7 is used. The low-power high-speed operational amplifier U3 (AD8038) acts as a difference amplifier. The voltage difference across the shunt is amplified by a factor of 100, i.e., 1 A flowing through the shunt corresponds to 1 V. Furthermore, the reference voltage generated by V4 is reduced by a factor of 10, where the resulting value corresponds to the reference current through the 10 Ω load resistor. Overall, the output of the operational amplifier labeled *diff* represents the difference between the reference and the measured current. The PI controller is realized by the arbitrary behavioral voltage source B1, taking the output voltage of the operational amplifier as an input signal. The factor of 12 in the definition of B1 rescales the duty ratio to *In* a real circuit this controller would be implemented using an operational amplifier as well.



**Figure 17.** Implementation of closed-loop buck converter with a lossy transmission line in LTspice®.

Figure 18 shows the input current and the output load voltage of the transmission line resulting from the transient simulation of the closed-loop control system. Again, the circuit simulation shows a qualitative agreement with the high-level simulation results shown in Figure 16. As expected, the P controller yields a remaining offset, i.e., the reference voltage of 6 V is not reached. This offset is compensated in the case of the PI controller. In both cases, the voltages show no oscillations.



**Figure 18.** Closed-loop circuit simulation results: input current (left) and output voltage (right) using P and PI controller.

## 6. Discussion

In the paper, a buck converter was analyzed in which the inductor was replaced by a transmission line. Converter topologies with a transmission line are comparatively rarely discussed in the literature. In contrast to [2,3], the distributed converter model discussed in the article is not just an intermediate step for a different setup with several discrete components, but could be used in such a way that the power inductor can actually be saved. When compared to the models considered in previous papers [5–7], the model in this contribution also contains an external capacitor.

Converters with a transmission line are distributed-parameter systems described by PDEs. In general, there are two basic strategies for designing controllers for distributed systems. In the case of early lumping, the distributed system model is discretized, and then, the controller is designed. Classic design methods can be used for this purpose. In the case of late lumping, the controller is designed for the distributed model. This approach usually leads to a distributed controller model, which is then discretized for the implementation. This design approach is generally more difficult. The controller in [35] was derived in the time domain on the basis of a control Lyapunov functional and was then approximated for the implementation. The result is a nonlinear switching controller that excites the converter circuit in a very high frequency range. In this article, the controller design was based on an approximation of the plant's model in the frequency domain, resulting in a linear controller.

For DC/DC converters, linear controllers are fairly widespread, where the design is usually carried out in the frequency domain [16,24,36]. With a PI controller, a linear and comparatively easy to implement analog controller was used. In principle, implementation with a digital controller would also be possible. With this, however, the current measurement should be synchronized with the pulse-width modulation. More complex controller strategies could then be used, e.g., internal model control [37–39], nonlinear controllers [12–14] including model predictive control (MPC) [40], or control concepts based on artificial neural networks, as in [41]. In this case, however, the question arises as to whether the saving on the coil with the suggested topology justifies this additional expense.

Although the system dynamics of the RLC networks can be described by linear models, both in the lumped-parameter and the distributed-parameter case, the use of PWM produces an input saturation to the interval  $[0, 1]$ , and thus, an overall nonlinear model. Together with the integral part of the controller, windup can occur. Fortunately, the corresponding anti-windup measures, as described in [33], can also be implemented relatively easily in terms of circuitry.

The investigations in Section 4 show that the classical and the distributed converter have a similar amplitude response over a wide frequency range. The behavior of the distributed converter can be divided into two frequency ranges. On the one hand, the external capacitor leads to a significantly lower first resonance frequency compared to [6,7]. Theoretically, this resonance frequency could be lowered further with a larger capacitor.

From a practical point of view, however, this is not recommended, as larger capacitors in particular can change their characteristics dramatically depending on the frequency [42,43]. For this reason small capacitors are sometimes placed in parallel to large ones in order to improve the high-frequency behaviour. In this frequency range, the behavior of the distributed converter resulting from a transcendental transfer function can be adequately described by a Padé approximant having the same order as the rational transfer function of the classical converter. This frequency range is used for the approximation and the subsequent controller design. The alternating resonance and antiresonance frequencies in the higher-frequency range are caused by the transmission line. However, these frequencies can also be lowered by using a longer transmission line.

The circuit simulation reveals numerous problems that would have to be anticipated in a practical implementation. The comparatively high switching and resonance frequencies require very fast components. Nevertheless, each component (e.g., the driver circuit and an operational amplifier) will cause a time delay in the signals, and thus, change the phase response of the system. This reduces the stability margin of the control loop or causes the system to become unstable.

The coaxial cable used here is primarily intended for signal transmission and not for transmitting power. The coaxial cable was used because the parameters of this cable are very well known and it is also supported by circuit simulators. Experimental results on the open-loop control of the distributed buck converter shown in [6,7] show a good agreement with the simulation results. A twisted-pair cable would certainly make more sense for practical and economical implementation. Further research should be devoted to a practical circuit implementation of the suggested closed-loop control of the distributed buck converter, whereby the use of twisted-pair wires could also be investigated experimentally. Microstrips would also be conceivable for smaller implementations on a printed circuit board [44].

Of course, the question arises as to whether this approach could also be relevant for other types of switched-mode converters. If a supply line is to be used meaningfully as an inductor, in the conventional converter circuit the inductor must be in series between the power supply and the load. This, for example, does not apply to the buck–boost converter; see Figure 7 of [2] and Figure 2 of [3]. In addition, the manipulated variable and the feedback variable should be on the same side of the transmission line, as otherwise another signal line would be necessary. In this article, the left-hand side (supply side) was considered, whereby the voltage was fed in and the current was measured for the control. The right-hand side (load side) would be suitable for the boost converter [4]. The incorporation of transmission lines into the models can certainly also be of interest for applications in electric drives and power grids where AC and multilevel converters are used [8,45–47], which could be subject of further research.

**Author Contributions:** Conceptualization, K.R. and D.G.; methodology, D.G.; software, K.R.; validation, D.G.; formal analysis, K.R. and D.G.; writing—original draft preparation, K.R.; writing—review and editing, D.G.; visualization, K.R.; supervision, K.R.; All authors have read and agreed to the published version of the manuscript.

**Funding:** This research received no external funding.

**Institutional Review Board Statement:** Not applicable.

**Informed Consent Statement:** Not applicable.

**Data Availability Statement:** The source files for the simulations will be available on Github [26] under the GNU General Public License v3.0.

**Conflicts of Interest:** The authors declare no conflicts of interest.

## Abbreviations

The following abbreviations are used in this manuscript:

AC	Alternating current
DC	Direct current
ODE	Ordinary differential equation
PDE	Partial differential equation
BIBO	Bounded-input bounded-output
LTRA	Lossy transmission line model
P controller	Proportional controller
PI controller	Proportional–integral controller
MPC	Model predictive control

## References

- Bacha, S.; Munteanu, I.; Bratcu, A.I. *Power Electronic Converters Modeling and Control*; Springer: London, UK, 2014.
- Sander, S. Buck and boost converters with transmission lines. *IEEE Trans. Power Electron.* **2012**, *27*, 4013–4020. [[CrossRef](#)]
- Sander, S.; Karvonen, A. Semiconductor component reduction in AC/DC converters with transmission lines. In Proceedings of the 15th European Conference on Power Electronics and Applications (EPE), Lille, France, 2–6 September 2013; pp. 1–10.
- Röbenack, K.; Bärnklaus, H. A Spatially Distributed Boost Converter – Modeling and Simulation. In Proceedings of the International Conference on System Theory, Control and Computing (ICSTCC), Timisoara, Romania, 11–13 October 2023; pp. 480–486. [[CrossRef](#)]
- Huang, C.; Woittennek, F.; Röbenack, K. Steady-state analysis of a distributed model of the buck converter. In Proceedings of the European Conference on Circuit Theory and Design (ECCTD), Dresden, Germany, 8–12 September 2013; pp. 1–4. [[CrossRef](#)]
- Röbenack, K.; Herrmann, R. Analysis, Simulation and Implementation of a Distributed Buck Converter. In Proceedings of the 26th International Conference on System Theory, Control and Computing (ICSTCC), Sinaia, Romania, 19–21 October 2022; pp. 213–218. [[CrossRef](#)]
- Röbenack, K.; Herrmann, R. Distributed Buck Converter Realization Based on a Transmission Line. *Syst. Theory Control Comput. J.* **2023**, *3*, 29–35. [[CrossRef](#)]
- Zainea, M.; van der Schaft, A.; Buisson, J. Stabilizing control for power converters connected to transmission lines. In Proceedings of the Proc. American Control Conference (ACC), New York, NY, USA, 9–13 July 2007; pp. 3476–3481. [[CrossRef](#)]
- Daafouz, J.; Tucsnak, M.; Valein, J. Nonlinear control of a coupled PDE/ODE system modeling a switched power converter with a transmission line. *Syst. Control Lett.* **2014**, *70*, 92–99. [[CrossRef](#)]
- King, W.P. *Transmission Line Theory*; Dover Publications Inc.: New York, NY, USA, 1965.
- Mathis, W.; Reibiger, A. *Küpfmüller Theoretische Elektrotechnik*, 20th ed.; Springer Vieweg: Berlin/Heidelberg, Germany, 2017. [[CrossRef](#)]
- Sira-Ramírez, H. Nonlinear P-I Controller Design for Switchmode dc-to-dc power converters. *IEEE Trans. Circuits Syst.* **1991**, *38*, 410–417. [[CrossRef](#)]
- Escobar, G.; Ortega, R.; Sira-Ramírez, H.; Vilan, J.P.; Zein, I. An experimental comparison of several non linear controllers for power converters. *IEEE Control Syst.* **1999**, *19*, 66–82.
- Kugi, A.; Schlacher, K. Nonlinear  $H_\infty$ -Controller Design for a DC-to-DC Power Converter. *IEEE Trans. Control Syst. Technol.* **1999**, *7*, 230–237. [[CrossRef](#)]
- Duong, M.Q.; Sava, G.N.; Scripcariu, M.; Mussetta, M. Design and simulation of PI-type control for the Buck Boost converter. In Proceedings of the 2017 International Conference on Energy and Environment (CIEM), Bucharest, Romania, 19–20 October 2017; pp. 79–82. [[CrossRef](#)]
- Garg, M.M.; Hote, Y.V.; Pathak, M.K.; Behera, L. An approach for buck converter PI controller design using stability boundary locus. In Proceedings of the 2018 IEEE/PES Transmission and Distribution Conference and Exposition (T&D), Denver, CO, USA, 16–19 April 2018; pp. 1–5. [[CrossRef](#)]
- Tzafestas, S.G. *Distributed Parameter Control Systems: Theory and Application*; International Series on Systems and Control; Pergamon Press: Oxford, UK, 2013; Volume 6.
- Christofides, P.D.; Daoutidis, P. Feedback control of hyperbolic PDE systems. *AIChE J.* **1996**, *42*, 3063–3086. [[CrossRef](#)]
- Deutscher, J.; Harkort, C. A parametric approach to finite-dimensional control of linear distributed-parameter systems. *Int. J. Control* **2010**, *83*, 1674–1685. [[CrossRef](#)]
- Eraydin, H.; Bakan, A.F. Efficiency comparison of asynchronous and synchronous buck converter. In Proceedings of the 6th International Conference on Electric Power and Energy Conversion Systems (EPECS), Istanbul, Turkey, 5–7 October 2020; pp. 30–33. [[CrossRef](#)]
- Dimirovski, G.; Gough, N.; Barnett, S. Categories in systems and control theory. *Int. J. Syst. Sci.* **1977**, *8*, 1081–1090. [[CrossRef](#)]
- TimKabel. RG 58 C/U 50  $\Omega$ , Coaxial Cable. Available online: [http://www.tim-kabel.hr/images/stories/katalog/datasheetHRV/1502\\_RG58\\_ENG.pdf](http://www.tim-kabel.hr/images/stories/katalog/datasheetHRV/1502_RG58_ENG.pdf) (accessed on 8 May 2023).

23. LAPP. RG-58 C/U. 2020. Available online: <https://e.lapp.com/apac/p/coaxial-cables/coaxial-rg-58-c-u-2170000> (accessed on 25 January 2024).
24. Erickson, R.W.; Maksimovic, D. *Fundamentals of Power Electronics*, 3rd ed.; Springer Nature Switzerland AG: Cham, Switzerland, 2007. [CrossRef]
25. Scilab. Available online: <http://www.scilab.org/> (accessed on 5 January 2024).
26. Current-Mode Control of a Distributed Buck Converter with a Lossy Transmission Line, Scilab Source Files. Available online: <https://github.com/TUD-RST/current-mode-control-buck-converter> (accessed on 31 August 2024).
27. LTspice®. Available online: <https://www.analog.com/en/resources/design-tools-and-calculators/ltspice-simulator.html> (accessed on 31 August 2024).
28. Maxima, a Computer Algebra System. Available online: <http://maxima.sourceforge.net> (accessed on 10 January 2024).
29. The Sage Developers. SageMath, the Sage Mathematics Software System (Version 10.2). 2024. Available online: <https://www.sagemath.org> (accessed on 10 January 2024).
30. Marlin, T.E. *Process Control, Designing Processes and Control Systems for Dynamics Performance*, 2nd ed.; McGraw-Hill: Boston, MA, USA, 2000.
31. O'Dwyer, A. *Handbook of PI and PID Controller Tuning Rules*; Imperial College Press: London, UK, 2009.
32. Dutoon, K.; Thompson, S.; Barraclough, B. *The Art of Control Engineering*; Addison-Wesley: Harlow, UK, 1997.
33. Hippe, P. *Windup in Control: Its Effects and Their Prevention*; Springer: London, UK, 2006.
34. Zhou, K.; Doyle, J.C. *Essentials of Robust Control*; Prentice Hall: Upper Saddle River, NJ, USA, 1998.
35. Röbenack, K.; Palis, S. Set-Point Control of a Spatially Distributed Buck Converter. *Algorithms* **2023**, *16*, 55. [CrossRef]
36. Linear Technology. *OPTI-LOOP Architecture Reduces Output Capacitance and Improves Transient Response*; Application Note 76; Linear Technology: Milpitas, CA, USA, 1999.
37. Economou, C.G.; Morari, M. Internal Model Control. 5. Extension to Nonlinear Systems. *Ind. Eng. Chem. Process Des. Dev.* **1986**, *25*, 403–411. [CrossRef]
38. Henson, M.A.; Seborg, D.E. An internal model control strategy for nonlinear systems. *AIChE J.* **1991**, *37*, 1065–1081. [CrossRef]
39. Datta, A. Internal Model Control Schemes. In *Adaptive Internal Model Control*; Springer: London, UK, 1998; pp. 47–58.
40. Lin, H.; Chung, H.S.H.; Shen, R.; Xiang, Y. Enhancing Stability of DC Cascaded Systems With CPLs Using MPC Combined with NI and Accounting for Parameter Uncertainties. *IEEE Trans. Power Electron.* **2024**, *39*, 5225–5238. [CrossRef]
41. Xiang, Y.; Chung, H.S.H.; Lin, H. Light implementation scheme of ANN-based explicit model-predictive control for DC–DC power converters. *IEEE Trans. Ind. Inform.* **2023**, *20*, 4065–4078. [CrossRef]
42. Parler, S.G. Improved Spice models of aluminum electrolytic capacitors for inverter applications. In Proceedings of the Conference Record of the 2002 IEEE Industry Applications Conference, 37th IAS Annual Meeting (Cat. No. 02CH37344), Pittsburgh, PA, USA, 13–18 October 2002; Volume 4, pp. 2411–2418. [CrossRef]
43. Makdessi, M.; Sari, A.; Venet, P. Improved model of metalized film capacitors. *IEEE Trans. Dielectr. Electr. Insul.* **2014**, *21*, 582–593. [CrossRef]
44. Lacoste, R. *Robert Lacoste's The Darker Side: Practical Applications for Electronic Design Concepts from Circuit Cellar*; Newnes: Oxford, UK, 2009.
45. Lupo, G.; Petrarca, C.; Vitelli, M.; Tucci, V. Multiconductor transmission line analysis of steep-front surges in machine windings. *IEEE Trans. Dielectr. Electr. Insul.* **2002**, *9*, 467–478. [CrossRef]
46. Bärnklaus, H.; Gensior, A.; Rudolph, J. A model-based control scheme for modular multilevel converters. *IEEE Trans. Ind. Electron.* **2012**, *60*, 5359–5375. [CrossRef]
47. Xie, Y.; Zhang, J.; Leonardi, F.; Munoz, A.R.; Degner, M.W.; Liang, F. Modeling and verification of electrical stress in inverter-driven electric machine windings. *IEEE Trans. Ind. Appl.* **2019**, *55*, 5818–5829. [CrossRef]

**Disclaimer/Publisher's Note:** The statements, opinions and data contained in all publications are solely those of the individual author(s) and contributor(s) and not of MDPI and/or the editor(s). MDPI and/or the editor(s) disclaim responsibility for any injury to people or property resulting from any ideas, methods, instructions or products referred to in the content.